Experimental Determination of Electronic States via Digitized Shortcut to Adiabaticity and Sequential Digitized Adiabaticity

Ze Zhan,[1,§] Chongxin Run,[1,§] Zhiwen Zong,[1] Liang Xiang,[1] Ying Fei,[1] Zhenhai Sun,[1] Yaozu Wu,[1] Zhilong Jia ,[2] Peng Duan,[2] Jianlan Wu,[1,*] Yi Yin ,[1,†] and Guoping Guo[2,3,‡]

[1]*Zhejiang Province Key Laboratory of Quantum Technology and Device, Department of Physics, Zhejiang University, Hangzhou 310027, China*

[2]*Key Laboratory of Quantum Information, University of Science and Technology of China, Hefei 230026, China*

[3]*Origin Quantum Computing, Hefei 230026, China*

A combination of digitized shortcut to adiabaticity (STA) and sequential digitized adiabaticity is implemented in a superconducting quantum device to determine the electronic states in two example systems, the H_2 molecule and the topological Bernevig-Hughes-Zhang (BHZ) model. For H_2, a short internuclear distance is chosen as a starting point, at which the ground and excited states are obtained via digitized STA. From this starting point, a sequence of internuclear distances is built. The eigenstates at each distance are sequentially determined from those at the previous distance via the digitized adiabaticity, leading to the potential energy landscapes of H_2. The same approach is applied to the BHZ model and the valence and conduction bands are obtained with a high degree of accuracy along the X-Γ-X line cut of the first Brillouin zone. Furthermore, a numerical simulation of this method is performed to successfully extract the ground states of hydrogen chains with lengths of between three and six atoms.

I. INTRODUCTION

The rapid advancement in quantum computation has shed the light on rich practical applications [1–4]. In a conventional computer, the computational burden of an electronic state increases exponentially with the system size. The evolution of a quantum state in a quantum computing device can circumvent the difficulty of searching for a multidimensional Hilbert space [1]. The electronic ground state can be determined by the criterion of the lowest energy, according to which a variational quantum eigensolver (VQE) protocol has been proposed for a quantum computing device [5–8]. The VQE has been experimentally implemented to calculate various systems ranging from small molecules (e.g., H_2 [6], LiH, and BeH_2 [7]), to an atom chain of H_{12} [8]. Due to the intrinsic requirement of energy minimization, it is more difficult to calculate the electronic excited states with VQE. In a recent experiment, the excited eigenstates of H_2 have been determined in a space composed of local states excited from the ground state [9].

An important family of quantum computing methods is rooted in quantum adiabaticity [10–21]. A quantum system evolves along its instantaneous eigenstate under a slowly varying Hamiltonian and both dynamic and geometric phases are accumulated over time. Alternatively, a shortcut-to-adiabaticity (STA) is designed to accelerate the adiabatic process with the assistance of a counterdiabatic Hamiltonian [22–35]. In superconducting quantum devices, the experimental implementation of the STA has been well studied in a single-qubit system [26–30] but it becomes difficult in multiqubit systems, where the exact form of the counterdiabatic Hamiltonian is often complicated. Recently, a single-qubit approximation [33] and a sum of nested commutators [34] have been proposed to simplify the estimation of the counterdiabatic Hamiltonian. The realization of a time-varying multiqubit Hamiltonian is, however, an experimentally nontrivial task. On the other hand, digital quantum computing based on the Trotter-Suzuki decomposition offers a universal tool for various quantum problems [36–39]. With continual improvement in equipments and algorithms, digital quantum computing has gradually become practically available. For example, the digitized adiabatic [18–21] and STA [33] algorithms have been proposed and tested in the preparation of entangled multiqubit states.

To fully understand the electronic structure of a quantum system, the eigenstates and eigenenergies need to

---

034050-1

be determined over a whole parameter space. A potential energy landscape of a microscopic system can lead to its molecular structure or to relevant reaction pathways. The electronic band structure of a crystal system is essential for electromagnetic properties. With the development of various eigensolvers, we may determine the eigenstates repeatedly via the same method as for the parameter changes. Instead, the historical information collected over the eigensolving process can be utilized for a later state determination. In particular, we introduce a method of sequential digitized adiabaticity. For a preselected parameter sequence, the eigenstates at each position can be determined by a digitized adiabatic evolution from the eigenstates predetermined at the previous position. Due to the short distance between two adjacent positions, the adiabatic process can be sufficiently reliable over a short operation time. In this paper, we apply the combination of digitized STA and sequential digitized adiabaticity to experimentally determine the potential energy landscapes (both the ground and first excited states) of H_2 and the valence and conduction bands along the X-Γ-X line cut for the topological Bernevig-Hughes-Zhang (BHZ) model [40]. Furthermore, we explore the ground-state energy landscapes of multiatom hydrogen chains by a numerical simulation.

II. THEORY

A digitized adiabatic or STA eigensolver is rooted in an adiabatic process (see Fig. 1). To extract the eigenenergies and eigenstates $\{\varepsilon_n, |\varphi_n\rangle\}$ of a target Hamiltonian H, we begin with an initial Hamiltonian H_0 and design a time-varying Hamiltonian,

$$H_{\mathrm{ad}}(t) = H_0 + \lambda(t)(H - H_0), \qquad (1)$$

where the coefficient satisfies $\lambda(t = 0) = 0$ at the initial time and $\lambda(t = T) = 1$ at the final time. If the initial state is an eigenstate, $|\Psi(t = 0)\rangle = |\varphi_n(H_0)\rangle$ and the Hamiltonian varies extremely slowly, $|\dot\lambda(t)| \to 0$, the adiabatic evolution spontaneously drags the quantum system to its final eigenstate, $\lim_{T \to \infty} |\Psi(t = T)\rangle = U_{\mathrm{ad}}|\Psi(0)\rangle = \exp[i\Phi_n(T)]|\varphi_n(H)\rangle$. Here, $U_{\mathrm{ad}} = \exp_+[-i\int_0^T H_{\mathrm{ad}}(\tau)d\tau]$ is the time-evolution operator and the phase $\Phi_n(T)$ includes both dynamic and geometric parts. The reduced Planck constant $\hbar$ is set to be unity throughout this paper.

For the STA process, a counterdiabatic Hamiltonian is introduced as [22–35]

$$H_{\mathrm{cd}}(t) = i\sum_n [|\dot\varphi_n(t)\rangle\langle\varphi_n(t)| - \langle\varphi_n(t)|\dot\varphi_n(t)\rangle|\varphi_n(t)\rangle\langle\varphi_n(t)|],$$

$$(2)$$

where $|\varphi_n(t)\rangle \equiv |\varphi_n(H_{\mathrm{ad}}(t))\rangle$ is the nth instantaneous eigenstate of the adiabatic Hamiltonian $H_{\mathrm{ad}}(t)$. For a
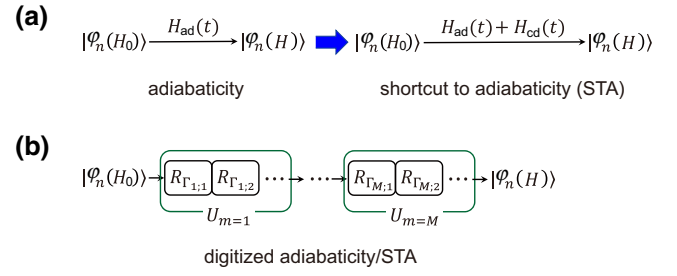

FIG. 1. A schematic diagram of the (a) continuous and (b) digitized adiabatic or STA processes.

finite operation time T, the quantum system subject to the total Hamiltonian $H_{\mathrm{tot}}(t) = H_{\mathrm{ad}}(t) + H_{\mathrm{cd}}(t)$ is dragged exactly to the eigenstate $|\Psi(t = T)\rangle = U_{\mathrm{STA}}|\Psi(0)\rangle = \exp[i\Phi'_n(T)]|\varphi_n(H)\rangle$ under the conditions of $\dot\lambda(0) = 0$ and $\dot\lambda(T) = 0$. The time-evolution operator is changed to be $U_{\mathrm{STA}} = \exp_+[-i\int_0^T H_{\mathrm{tot}}(\tau)d\tau]$. Although the counterdiabatic Hamiltonian has been derived under various frameworks, e.g., the elimination of the nonadiabatic transition [22–34] and the Lewis-Riesenfeld invariant [35], $H_{\mathrm{cd}}(t)$ can recover the same expression as in Eq. (2).

From a practical perspective, the adiabatic process usually needs a long operation time, i.e., $\varepsilon T_{\min} \gg 1$, where ε is a characteristic energy of the system and $T_{\min}$ is the minimum value of T for the output fidelity above a threshold. The STA can accelerate the adiabatic process but the appearance of instantaneous eigenstates in Eq. (2) contradicts our ultimate goal of determining $|\varphi_n(H)\rangle$. To avoid this problem, we apply a single-qubit assumption in the scenario of a weak interqubit interaction (for details, see Appendix A and Sec. III) [33,34]. The operation time of this approximate STA can be compressed to satisfy $\varepsilon T_{\min} \lesssim O(1)$. With the increase of the interqubit interaction and in the case of a multiqubit interaction, a more systematic treatment is an expansion over nested commutators [34]. Instead, we reselect a more appropriate initial Hamiltonian H_0 to suppress the Hamiltonian deviation $\|H - H_0\|$ and the state distance between $|\varphi_n(H)\rangle$ and $|\varphi_n(H_0)\rangle$. The adiabatic prediction is practically reliable under a short operation time $[\varepsilon T_{\min} \lesssim O(1)]$ without the necessity for the STA.

The experimental realization of a time-varying multiqubit Hamiltonian (adiabatic or STA) is possible but difficult. Instead, a digitized algorithm can realize the time evolution of an arbitrary Hamiltonian [18–21,33]. After dividing the operation time into M segments ($\Delta t = T/M$), we apply the Trotter-Suzuki decomposition [36–39] to the time-evolution operator ($U = U_{\mathrm{ad}}$ or U_{STA}), which leads to

$$U \approx U_M \cdots U_2 U_1, \qquad (3)$$

with $U_{m=1,\dots,M} = \exp[-iH_{\mathrm{ad/tot}}(m\Delta t)\Delta t]$. In general, the adiabatic or total Hamiltonian can be expanded into

$H_{ad/tot}(t) = \sum_{j=1}^{J} \omega_j(t)\Gamma_j/2$, where Γ_j is a quantum operator, $\omega_j(t)$ is its associated coefficient, and J is the total number of operators. The Trotter-Suzuki decomposition allows a new factorization [36–39],

$$U_m \approx R_{\Gamma_J}(\theta_{m;J}) \cdots R_{\Gamma_2}(\theta_{m;2}) R_{\Gamma_1}(\theta_{m;1}) \quad (4)$$

where $R_{\Gamma_j}(\theta_{m;j}) = \exp[-i\theta_{m;j}\Gamma_j/2]$ can be viewed as a generalized rotation operator over an angle $\theta_{m;j} = \omega_j(m\Delta t)\Delta t$. In practice, $R_{\Gamma_j}(\theta_{m;j})$ can be realized by a combination of sequential single- and two-qubit gates. Note that the real experimental time is determined by the total time of the gates rather than the adiabatic or STA operation time T.

III. EXPERIMENTAL REALIZATION

The digitized adiabatic and STA eigensolvers are implemented in a quantum computing device composed of six superconducting cross-shaped transmon qubits [41], from which two qubits (Q_A and Q_B) are selected. The ground and excited states of each qubit are mapped onto the up and down states of a spin, i.e., $|0\rangle \leftrightarrow |+\rangle$ and $|1\rangle \leftrightarrow |-\rangle$. The device is mounted in an aluminum sample box and in a dilution refrigerator with a base temperature around 10 mK. The frequency-tunable qubits are initially biased at an operation point through two Z control lines. In our experiment, the two qubits are set at $\omega_A/2\pi = 6.21$ GHz and $\omega_B/2\pi = 5.70$ GHz. The two anharmonicity parameters are $\Delta_A/2\pi \approx \Delta_B/2\pi = -250$ MHz, enabling a selective microwave drive to control each qubit through its X-Y control line. At the operation point, the relaxation times are $T_{A;1} = 5.8$ μs and $T_{B;1} = 6.9$ μs, while the pure dephasing times are $T_{A;\phi} = 26$ μs and $T_{B;\phi} = 28$ μs. The readout fidelities of the ground and the excited states are $F_{A;0} = 99\%$ and $F_{A;1} = 95\%$ for qubit A, and $F_{B;0} = 97\%$ and $F_{B;1} = 93\%$ for qubit B [42].

A. Hydrogen molecule

Under the Born-Oppenheim approximation, the electronic Hamiltonian of a hydrogen molecule is written as

$$H(\vec{r}_1, \vec{r}_2 | \vec{R}_1, \vec{R}_2) = \mathcal{E}_{nucl}(R) + \sum_{i=1,2} \frac{\vec{p}_i^2}{2m}$$
$$- \sum_{i,j=1,2} \frac{e^2}{4\pi\varepsilon_0 |\vec{r}_i - \vec{R}_j|} + \frac{e^2}{4\pi\varepsilon_0 |\vec{r}_1 - \vec{r}_2|}, \quad (5)$$

where $\vec{p}_{i=1,2}$ and $\vec{r}_{i=1,2}$ are the momenta and coordinates of two electrons and $\vec{R}_{i=1,2}$ are the coordinates of two nuclei. The nuclear term $\mathcal{E}_{nucl}(R)$ is dependent on the internuclear distance $R = |\vec{R}_1 - \vec{R}_2|$. For the ground and

several lowest excited electronic states of H_2, the single-electron basis functions are combined by two delocalized orbitals $\{|\phi_g\rangle, |\phi_u\rangle\}$ and two spin states $\{|+\rangle, |-\rangle\}$, i.e., $|\chi_{i=1,\ldots,4}(\vec{r}, \sigma)\rangle = |\phi_{g/u}(\vec{r})\rangle \otimes |\sigma = +/-\rangle$ with $\vec{r}$ and σ the coordinate and spin variables [5,6,9]. In the number representation with regard to $\{|\chi_i\rangle\}$, the second quantization of the Hamiltonian is $H = \mathcal{E}_{nucl} + \sum h_{ij} a_i^+ a_j + \sum h_{ijkl} a_i^+ a_j^+ a_k a_l$, where a_i and a_i^+ are annihilation and creation operators satisfying $[a_i, a_j^+]_+ = \delta_{i,j}$. The single- and two-electron integrals (h_{ij} and h_{ijkl}) depend on the internuclear distance R [5,6,9]. As shown in Appendix B, the Bravyi-Kitaev transformation [43] is applied and the target Hamiltonian is approximated as

$$H = g_0 + gZ_A + gZ_B + g_{12}Y_A Y_B, \quad (6)$$

where $\{X_\alpha, Y_\alpha, Z_\alpha\}$ is the set of Pauli matrices ($\alpha = A, B$) and the parameters $\{g_0, g, g_{12}\}$ are functions of R [5,6,9].

In the first step, we explore the ground state $|\varphi_0(H)\rangle$ at $R = 0.05$ Å, where the energy parameters are $g_0 = 10.08$ E_h, $g = -1.055$ E_h, and $g_{12} = 0.1557$ E_h ($E_h \approx 27.2$ eV) [9]. The initial Hamiltonian is selected to be $H_0 = g(Y_A + Y_B)$ and the adiabatic Hamiltonian $H_{ad}(t) = H_0 + \lambda(t)(H - H_0)$ is given by Eq. (1). The time-adjusting coefficient is set to be $\lambda(0 \leq t \leq T) = \sin^2(\pi t/2T)$ and this form is applied to all the experiments and numerical simulations in this paper. The initial ground state $|\varphi_0(H_0)\rangle = (|0\rangle + i|1\rangle)_A(|0\rangle + i|1\rangle)_B/2$ is experimentally generated by applying the $R_{X_A}(-\pi/2)$ and $R_{X_B}(-\pi/2)$ gates onto the two-qubit state $|00\rangle$. Due to the condition of $|g_{12}| \ll |g|$, the two-qubit coupling is separated into $Y_A Y_B \approx Y_A + Y_B$ under the single-qubit approximation. This simple approximation is applicable to a weak multiqubit interaction, although a nested-commutator expansion can improve the accuracy of the estimated H_{cd} with an increased computational burden (see Appendix A) [33,34]. Accordingly, the counterdiabatic Hamiltonian is approximated as $H_{cd}(t) \approx g_{cd}(t)(X_A + X_B)$ with $g_{cd}(t) = \dot{\lambda}(t)/[2\zeta^2(t) + 2\lambda^2(t)]$ and $\zeta(t) = 1 - (1 - g_{12}/g)\lambda(t)$. With both the adiabatic part $H_{ad}(t)$ and the counterdiabatic part $H_{cd}(t)$, the total Hamiltonian is rearranged into

$$H_{tot}(t) \approx \lambda(t)g_0 + \frac{\omega_1(t)}{2}Y_A Y_B + \frac{\omega_2(t)}{2}(Y_A + Y_B)$$
$$+ \frac{\omega_3(t)}{2}(X_A + X_B) + \frac{\omega_4(t)}{2}(Z_A + Z_B), \quad (7)$$

where $\omega_1(t) = 2\lambda(t)g_{12}$, $\omega_2(t) = 2[1 - \lambda(t)]g$, $\omega_3(t) = 2g_{cd}(t)$, and $\omega_4(t) = 2\lambda(t)g$. The STA operation time is empirically selected to be $gT \approx 0.8$, which is much shorter than that for an adiabatic process ($gT_{min} \approx 9$). The whole time evolution of the M-step digitized STA is given by Eq. (3) and each mth partial time-evolution operator is set to
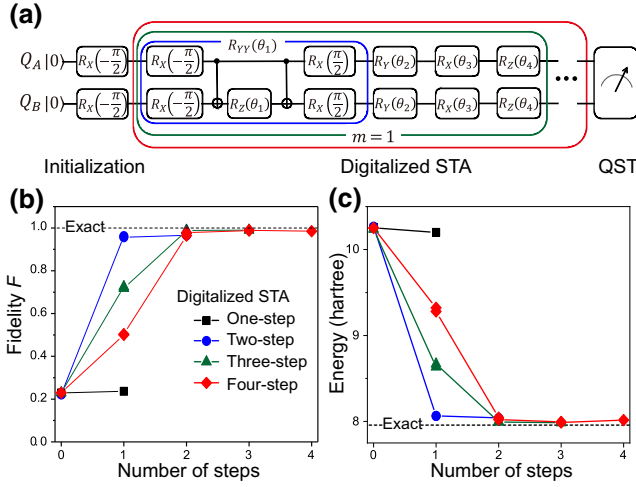
(a)

(b)   **(c)**

FIG. 2. The determination of the ground state of H_2 via a digitized STA eigensolver for the internuclear distance at $R = 0.05$ Å. (a) A quantum circuit diagram of the M-step digitized STA process. (b) The evolution of the state fidelities (in comparison to the exact ground state) in four digitized STA experiments ($1 \leq M \leq 4$). (c) The evolution of the state energies in four digitized STA experiments. The square, circle, triangle, and diamond denote the total number $M = 1, 2, 3, 4$ of digitized steps, respectively.

be

$$U_m = R_{Z_A}(\theta_{m;4})R_{Z_B}(\theta_{m;4})R_{X_A}(\theta_{m;3})R_{X_B}(\theta_{m;3})$$
$$\times R_{Y_A}(\theta_{m;2})R_{Y_B}(\theta_{m;2})R_{Y_A Y_B}(\theta_{m;1}), \qquad (8)$$

with

$$\begin{cases} \theta_{m,1} &= 2\lambda(m\Delta t)g_{12}\Delta t, \\ \theta_{m,2} &= 2[1 - \lambda(m\Delta t)]g\Delta t, \\ \theta_{m,3} &= 2g_{cd}(m\Delta t)\Delta t, \\ \theta_{m,4} &= 2\lambda(m\Delta t)g\Delta t. \end{cases} \qquad (9)$$

The two-qubit rotation $R_{Y_A Y_B}(\theta)$ in Eq. (8) is experimentally realized by [39]

$$R_{Y_A Y_B}(\theta) = R_{X_A}(\pi/2)R_{X_B}(\pi/2)U_{CN}R_{Z_B}(\theta)U_{CN}R_{X_A}$$
$$(-\pi/2)R_{X_B}(-\pi/2), \qquad (10)$$

where U_{CN} denotes a two-qubit controlled-NOT (CNOT) gate. The corresponding pulse sequence is shown in Fig. 2(a). In practice, we perform the digitized STA experiment up to four steps ($1 \leq M \leq 4$).

In our experiment on superconducting qubits, errors occur during the initialization, operation, and measurement. For example, the input pulse is generated by a digital-to-analog converter (DAC), so that the pulse experienced by qubits can deviate from the designed shape due to the filtering effect. A single STA step in Eq. (8) involves

11 single-qubit gates and two two-qubit gates and the operation error can quickly accumulate through an M-step STA process. Due to the nature of a transmon qubit, the error is unavoidable in the state measurement. In addition to a careful calibration, we introduce three approaches to further correct errors and achieve a reliable output. (1) At each mth step, the starting state $|\Psi((m-1)\Delta t)\rangle$ is reprepared by a two-qubit universal quantum circuit (four rotation gates and one CNOT gate) [44] after it is experimentally determined in the previous $(m-1)$th step. Our modification is equivalent to an evolution of $|\Psi(0)\rangle \rightarrow |\Psi((m-1)\Delta t)\rangle \rightarrow |\Psi(m\Delta t)\rangle$, which can largely suppress the error accumulation in the pathway of $|\Psi(0)\rangle \rightarrow |\Psi(\Delta t)\rangle \rightarrow \cdots \rightarrow |\Psi((m-1)\Delta t)\rangle$. For an $N(> 2)$-qubit system, the universal quantum circuit can become difficult but a single-step production of $|\Psi(0)\rangle \rightarrow |\Psi((m-1)\Delta t)\rangle$ is practically possible. In the VQE protocol, the state determination of $|\Psi(0)\rangle \rightarrow |\Psi(H)\rangle$ is a single-step operation, although the rotation angles vary step by step [5–9]. (2) At each mth step, the rotation angles $\{\theta_{m;j}\}$ in Eq. (9) are adjusted to improve the reliability of U_m, since the overall effect of various errors behaves as a "phase error" in our generalized rotation operators. The angle adjustment is, in general, a small value ($\lesssim 5°$) around its theoretical design and a similar experimental technique can be found in a previous VQE experiment of the hydrogen molecule [6]. (3) Due to the limitations of our current experimental setup, the previous two approaches cannot fully remove the errors, so we apply a state purification approach as follows. For an arbitrary mixed state, the density matrix can be diagonalized and expanded into $\rho_{\exp}(t) = \sum_i P_i(t)|\psi_i(t)\rangle\langle\psi_i(t)|$, where $|\psi_i(t)\rangle$ is a pure state and $P_i(t)$ is its population. We expect that the state evolution is not far away from the theoretical simulation. The state $|\psi_i(t)\rangle$ with the largest population is thus considered to be an error-corrected experimental result. To visualize the influence of the error correction, we sequentially measure the starting and ending density matrices, $\rho((m-1)\Delta t)$ and $\rho(m\Delta t)$, with quantum state tomography (QST). Next we calculate a fidelity function,

$$\mathcal{S} = \langle \Psi_{theo}(t)|\rho_{\exp}(t)|\Psi_{theo}(t)\rangle, \qquad (11)$$

between the experimental result $\rho_{\exp}(t)$ and the theoretical simulation $|\Psi_{theo}(t)\rangle\langle\Psi_{theo}(t)|$ at the starting time $t = (m-1)\Delta t$ and the ending time $t = m\Delta t$. The propagation results of $\mathcal{S}$ for the M-step digitized STA ($1 \leq M \leq 4$) are shown in Fig. 3. Except for $|\Psi(0)\rangle$, the starting state $|\Psi((m-1)\Delta t)\rangle$ generated by the universal quantum circuit exhibits an approximately 5% error and a one-step digitized STA results in an extra 5–10% error for the ending state $|\Psi(m\Delta t)\rangle$. After purification, the state fidelities of $\mathcal{S}$ are consistently improved, becoming $> 99\%$. The above three treatments are also used in other experiments in this paper but may be unnecessary with the future improvement of sample quality and control accuracy.
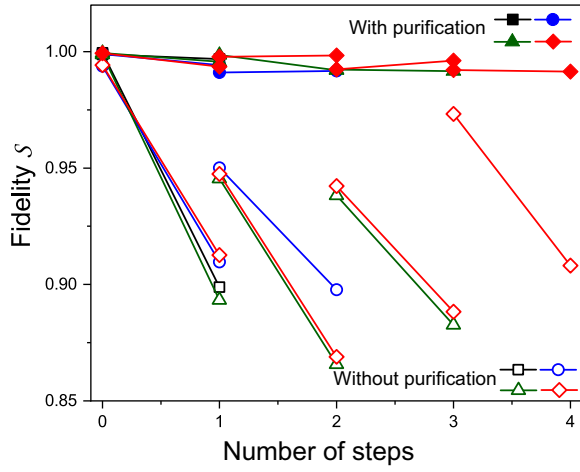
FIG. 3. The fidelity of the experimental density matrix $\rho_{exp}(t)$ in comparison to the theoretical simulation $|\Psi_{theo}(t)\rangle\langle\Psi_{theo}(t)|$ for the experiment shown in Fig. 2. The open symbols represent the results without state purification. The solid symbols represent the results by selecting the pure state $|\psi_i(t)\rangle$ with the largest population after the diagonalization of $\rho_{exp}(t)$. The square, circle, triangle, and diamond denote the total number $M = 1, 2, 3, 4$ of digitized steps, respectively.

Next, we present the time evolution of the error-corrected experimental result $|\Psi(t = m\Delta t)\rangle$ in comparison to the exact ground state $|\varphi_0(H)\rangle$. Similarly, another fidelity function,

$$\mathcal{F}_m = |\langle\varphi_0(H)|\Psi(t = m\Delta t)\rangle|^2, \quad (12)$$

is introduced for a quantitative description and the experimental results of $\mathcal{F}_m$ are presented in Fig. 2(b). For $M \geq 2$, the digitized STA efficiently drags the initial state ($\mathcal{F}_0 = 23\%$) to the exact state (the best fidelity $\mathcal{F}_M \approx 99\%$). We also calculate the state energies $E_m = \langle\Psi(m\Delta t)|H|\Psi(m\Delta t)\rangle$ through each M-step process [see Fig. 2(c)]; the experimental extraction is almost the same as the exact value $\varepsilon_0(R = 0.05 \text{ Å}) = 7.96 E_h$.

In the second step, we explore the first excited state $|\varphi_{n=1}(H)\rangle$ at $R = 0.05$ Å, while the other two excited states can be investigated similarly. The initial Hamiltonian is changed to be $H_0 = gZ_A$ and the initial state $|\Psi(0)\rangle = |01\rangle$ is obtained by applying the $R_{X_B}(\pi)$ gate to the state $|00\rangle$. Following the same procedure as above, a short operation time is selected to be $gT \approx 4.0$ and each mth partial time-evolution operator in the digitized STA is given by

$$U_m = R_{X_A}(\theta_{m;4})R_{Z_A}(\theta_{m;3})R_{Z_B}(\theta_{m;2})R_{Y_A Y_B}(\theta_{m;1}), \quad (13)$$

with

$$\begin{cases} \theta_{m,1} &= 2\lambda(m\Delta t)g_{12}\Delta t, \\ \theta_{m,2} &= 2g\Delta t, \\ \theta_{m,3} &= 2\lambda(m\Delta t)g\Delta t, \\ \theta_{m,4} &= 2g_{cd}(m\Delta t)\Delta t, \end{cases} \quad (14)$$
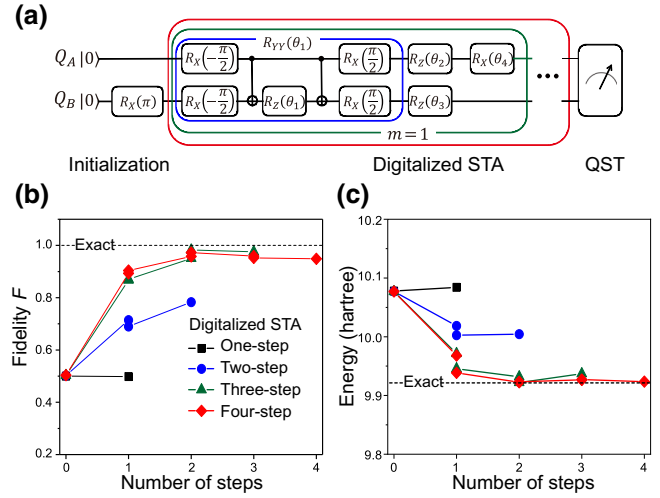

FIG. 4. The determination of the first excited state of H_2 via a digitized STA eigensolver for the internuclear distance at $R = 0.05$ Å. (a) A quantum circuit diagram of the M-step digitized STA process. (b) The evolution of the state fidelities in four digitized STA experiments ($1 \leq M \leq 4$) in comparison with the exact result. (c) The evolution of the state energies in four digitized STA experiments. The square, circle, triangle, and diamond denote the total number $M = 1, 2, 3, 4$ of digitized steps, respectively.

and $g_{cd}(t) = -\dot{\lambda}(t)gg_{12}/[2g + 2g_{12}\lambda^2(t)]$. The corresponding pulse sequence is plotted in Fig. 4(a). The experimental results of the state fidelity $\mathcal{F}_m = |\langle\varphi_{n=1}(H)|\Psi(m\Delta t)\rangle|^2$ and the state energy E_m are presented in Figs. 4(b) and 4(c). Consistent with the behavior in the ground state, the digitized STA efficiently drags the initial state ($\mathcal{F}_0 = 50\%$) to the exact first excited state (the best fidelity $\mathcal{F}_M \approx 98\%$) for $M \geq 3$, leading to an excellent prediction of the eigenenergy at $\varepsilon_1(R = 0.05 \text{ Å}) = 9.92 E_h$.

In the final step, we explore the electronic states of H_2 for various internuclear distances R, i.e., $|\varphi_{n=0,1}(R)\rangle \equiv |\varphi_{n=0,1}(H(R))\rangle$. With the increase of R, the amplitude of $g(R)$ gradually decreases and eventually becomes smaller than $g_{12}(R)$. For the two initial Hamiltonians, $H_0 = g(Y_A + Y_B)$ and $H_0 = gZ_A$, the previous single-qubit approximation gradually fails. Instead of an expansion over nested commutators [34], we apply a sequential digitized adiabatic approach. In the range 0.05 Å $\leq R \leq 1.65$ Å, a sequence of internuclear distances is set as $\{R_0 = 0.05 \text{ Å}, R_1 = 0.15 \text{ Å}, \ldots, R_{16} = 1.65 \text{ Å}\}$, which satisfies $R_i = R_{i-1} + \Delta R$ and $\Delta R = 0.1$ Å. To obtain the electronic structure at the ith distance, the initial Hamiltonian is selected to be $H_0 = c(R_i)H(R_{i-1})$, with $c(R_i) = g_{12}(R_i)/g_{12}(R_{i-1})$, and the initial states are the corresponding ground and first excited states, $|\Psi(0)\rangle = |\varphi_{n=0,1}(R_{i-1})\rangle$, which have been determined at the previous $(i - 1)$th distance. The adiabatic Hamiltonian is given accordingly by $H_{ad}(t) = c(R_i)H(R_{i-1}) +$

$\lambda(t)[H(R_i) - c(R_i)H(R_{i-1})]$. Due to a relatively small deviation between $|\varphi_n(R_{i-1})\rangle$ and $|\varphi_n(R_i)\rangle$, the adiabatic evolution can converge quickly and in practice we choose a digitized adiabatic process to realize the eigensolver. In detail, the time-evolution operator of the digitized adiabaticity is set to be $U_{ad} = U_M \cdots U_m \cdots U_1$ and

$$U_{m=1,...,M} = R_{Y_A Y_B}(\theta_{m;2})R_{Z_A}(\theta_{m;1})R_{Z_B}(\theta_{m;1}). \quad (15)$$

The rotation angles are $\theta_{m;1} = 2g_\lambda(m\Delta t)\Delta t$ and $\theta_{m;2} = 2g_{12}(R_i)\Delta t$, where we introduce a function $g_\lambda(t) = \lambda(t)g(R_i) + [1 - \lambda(t)]c(R_i)g(R_{i-1})$. The pulse sequence of this digitized adiabatic evolution is shown in the inset of Fig. 5(a). The operation time is in the range $1.0 \leq gT \leq 1.6$. For the ground state $|\varphi_0(R_i)\rangle$, the numbers of digitized steps are $M = 2$ for $0.15 \text{ Å} \leq R_i \leq 1.05 \text{ Å}$ and $M = 5$ for $1.15 \text{ Å} \leq R_i \leq 1.65 \text{ Å}$. For the first excited state $|\varphi_1(R_i)\rangle$, the number of digitized steps is always $M = 2$. To reduce the accumulation of experimental errors, the initial states $|\varphi_n(R_{i-1})\rangle$ are repreprared according to the numerical-simulation result (including a systematic error from the sequential digitized adiabaticity) with the universal quantum circuit [44]. The experimental result of the sequential digitized adiabaticity is summarized in Figs. 5(a)–5(c). In the most relevant range around the equilibrium distance, the state fidelities of both the ground and first excited states satisfy $\mathcal{F}_M \gtrsim 98\%$. In the range of large distances ($1.05 \text{ Å} \leq R_i \leq 1.65 \text{ Å}$), the fidelity of the ground state is $\mathcal{F}_M \gtrsim 94\%$, while that of the first excited state is $\mathcal{F}_M \gtrsim 97\%$ [see Fig. 5(b)]. The fidelity drop is expected to slow down with the decrease of the distance deviation ΔR. The potential energy landscape extracted experimentally is plotted in Fig. 5(a), showing an excellent agreement with the theoretical prediction. An enlarged view of the energy landscape for $1.05 \text{ Å} \leq R_i \leq 1.65 \text{ Å}$ is shown in Fig. 5(c). We thus obtain an accurate description of the electronic structure of H_2 using a delicate and efficient design of digitized STA and sequential digitized adiabaticity.

B. Topological BHZ model

The BHZ model can be used to describe the quantum spin Hall effect in a two-dimensional square lattice (the lattice constant is a) [40]. For simplicity, we consider one s orbital and one p orbital at each lattice point. In addition to the intraorbital interactions, the spin-modulated and orientation-modulated interorbital interactions are included for the nearest-neighbor hopping. After a discrete Fourier transform, the tight-binding Hamiltonian in the momentum space is block diagonal against the wave vector $\vec{k}$, giving $H = \sum_{\vec{k}} H(\vec{k})$ and

$$H(\vec{k}) = \sum_{\gamma_1 = s,p} \sum_{\gamma_2 = s,p} \sum_{\sigma = \pm} |\vec{k}\gamma_1\sigma\rangle [H(\vec{k})]_{\gamma_1\sigma;\gamma_2\sigma} \langle\vec{k}\gamma_2\sigma|. \quad (16)$$
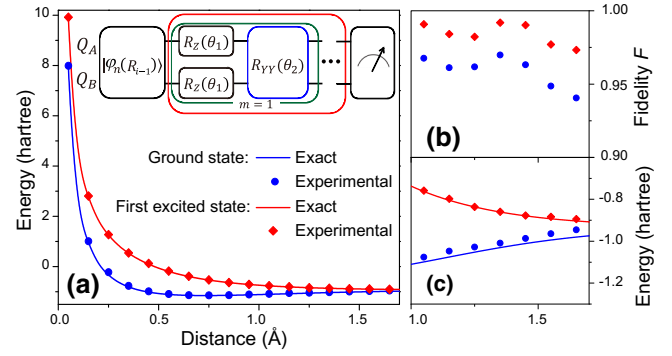

FIG. 5. The experimental determination of the potential energy landscapes for both the ground and excited states of H_2 via the digitized STA and sequential digitized adiabatic eigensolvers. (a) The two eigenergies ($\varepsilon_{n=0,1}$) as functions of the internuclear distance R. The quantum circuit diagram of a sequential digitized adiabaticity is shown in the inset. In the large-distance range ($1.05 \text{ Å} \leq R \leq 1.65 \text{ Å}$), the experimental results of the state fidelities and eigenenergies are enlarged in (b) and (c). The symbols (circles and diamonds) represent the experimental results, while the solid lines represent the exact results from the theoretical calculation.

By mapping the two orbitals $\{|s\rangle, |p\rangle\}$ onto a two-state spin, Eq. (16) is rearranged into

$$H(\vec{k}) = g_0(\vec{k}) + g(\vec{k})Z_B + \left[g_{12}(k_x)X_B + g_{12}(k_y)Y_B\right]Z_A, \quad (17)$$

where the subscripts A and B denote the spin and orbital degrees of freedoms, respectively. The coefficients are given explicitly by

$$\begin{cases} g_0(\vec{k}) &= C_1 f(\vec{k}), \\ g(\vec{k}) &= C_2 f(\vec{k}) - C_3, \\ g_{12}(h = k_x, k_y) &= C_4 \sin(ha), \end{cases} \quad (18)$$

where $f(\vec{k}) = 8[\sin^2(k_x a/2) + \sin^2(k_y a/2)]$. In our experiment, the three parameters are set to be $C_1 = 0.020$ eV, $C_2 = 0.027$ eV, $C_3 = 0.055$ eV, and $C_4 = 0.073$ eV from the HgTe/CdTe semiconductor quantum well [45]. The symmetry of H indicates twofold degenerate energy bands and a Dirac point at the Γ point ($k_x = k_y = 0$) of the first Brillouin zone (FBZ). To demonstrate the reliability of digitized STA and the sequential digitized adiabaticity, we drive the two-qubit system to determine the valence and conduction bands along the X-Γ-X line cut ($-\pi \leq k_x a < \pi$ and $k_y = 0$) in the FBZ.

Similar to the treatment in H_2, we first explore the electronic states $|\varphi_{n=0,1}(k_{x_0})\rangle \equiv |\varphi_n(H(k_x = k_{x_0}, k_y = 0))\rangle$ at two sets of starting points, one near the Γ point ($k_{x_0} = \pm 0.1a^{-1}$) and the other near the X point ($k_{x_0} = \pm 3.1a^{-1}$). For each wave vector, the initial Hamiltonian is selected to be $H_0 = g(k_{x_0})Z_B$. The initial ground state

of H_0 is $|\varphi_0(H_0)\rangle = |01\rangle$, generated by the $R_{X_B}(\pi)$ gate onto the two-qubit state $|00\rangle$, while the initial excited state is $|\varphi_1(H_0)\rangle = |00\rangle$. With respect to the adiabatic Hamiltonian, $H_{ad}(t) = H_0 + \lambda(t)(H - H_0)$, the counterdiabatic Hamiltonian $H_{cd}(t)$ is obtained under the single-qubit approximation, which is valid with the consideration of $|g_{12}(k_{x_0})| \ll |g(k_{x_0})|$. In M-step digitized STA, the partial time-evolution operator at each step is given by

$$U_m = R_{Z_B}(\theta_{m;3})R_{Y_B}(\theta_{m;2})R_{Z_A X_B}(\theta_{m;1}). \qquad (19)$$

with

$$\begin{cases} \theta_{m;1} &= 2\lambda(m\Delta t)g_{12}(k_{x_0})\Delta t, \\ \theta_{m;2} &= 2g_{cd}(k_{x_0}; m\Delta t)\Delta t, \\ \theta_{m;3} &= 2g(k_{x_0})\Delta t, \end{cases} \qquad (20)$$

and $g_{cd}(k_{x_0}; t) = \dot{\lambda}(t)g(k_{x_0})g_{12}(k_{x_0})/[2g(k_{x_0}) + 2g_{12}(k_{x_0})\lambda^2(t)]$. The corresponding pulse sequences for both the ground and excited states are shown in Figs. 6(a) and 6(b), respectively. In practice, we perform eight four-step digitized STA experiments ($0.5 \leq gT \leq 0.6$) and determine the corresponding eigenstates. For both $k_{x_0} = \pm 0.1a^{-1}$ and $\pm 3.1a^{-1}$, the experimental state fidelities of $|\varphi_{n=0,1}(k_{x_0})\rangle$ are around 98–99%.

Next, we explore the electronic states $|\varphi_{n=0,1}(k_x)\rangle$ at different wave vectors along the X-Γ-X line cut through the sequential digitized adiabaticity. With respect to each starting wave vector ($k_{x_0} = \pm 0.1a^{-1}, \pm 3.1a^{-1}$), a sequence of wave vectors, $\{k_{x_0}, k_{x_1}, \ldots, k_{x_i}, \ldots\}$, is assigned. For each sequence, the ending wave vector is at $k_x = \pm 1.6a^{-1}$ and the wave-vector deviation is $\Delta k_x = \pm 0.3a^{-1}$. In addition, we investigate two small wave vectors, $k_x = \pm 0.05a^{-1}$, using the reference points at $k_{x_0} = \pm 0.1a^{-1}$. At each ith wave vector k_{x_i}, the initial Hamiltonian is set to be $H_0 = c(k_{x_i})H(k_{x_{i-1}})$, where $c(k_{x_i}) = g_{12}(k_{x_i})/g_{12}(k_{x_{i-1}})$, while the initial state is $|\Psi(0)\rangle = |\varphi_{n=0,1}(k_{x_{i-1}})\rangle$. The adiabatic Hamiltonian is given by $H_{ad}(t) = c(k_{x_i})H(k_{x_{i-1}}) + \lambda(t)[H(k_{x_i}) - c(k_{x_i})H(k_{x_{i-1}})]$. In the M-step digitized adiabatic process, each partial time-evolution operator is given by

$$U_m = R_{Z_B}(\theta_{m;3})R_{Z_A X_B}(\theta_{m;2})R_{Z_B}(\theta_{m;1}), \qquad (21)$$

where $\theta_{m;1} = 2\Delta g(k_{x_i})\lambda(m\Delta t)\Delta t$, $\theta_{m;2} = 2g_{12}(k_{x_i})\Delta t$, and $\theta_{m;3} = 2c(k_{x_i})g(k_{x_{i-1}})\Delta t$. Here, we introduce a deviation function, $\Delta g(k_{x_i}) = g(k_{x_i}) - c(k_{x_i})g(k_{x_{i-1}})$. The pulse sequence of the digitized adiabaticity is shown in the inset of Fig. 6(c). The separation of $R_{Z_B}(\theta_1)$ and $R_{Z_B}(\theta_3)$ in Eq. (21) is found to yield a better performance than the combined case. The operation times are selected in the range $0.4 \leq gT \leq 1.8$. For $|k_x| \leq 1.0a^{-1}$ and the number of adiabatic steps is $M = 2$, while for $1.3a^{-1} \leq |k_x| \leq 2.8a^{-1}$, this number is changed to be $M = 5$. The experimental state fidelities of both the valence and conduction

bands along the X-Γ-X line cut satisfy $\mathcal{F}_M \gtrsim 98\%$. In Fig. 6(d), we plot the corresponding experimental band structures, $\varepsilon_{n=0,1}(k_x) = \langle \varphi_n(k_x)|H|\varphi_n(k_x)\rangle$, which are in excellent agreement with the theoretical prediction. In the inset of Fig. 6(d), we experimentally extract a linear dispersion relation, $\varepsilon_n(k_x) - 2C_1 \sim \pm C_4 k_x a$ around the Dirac point ($k_x = 0$).

IV. NUMERICAL SIMULATION OF HYDROGEN CHAINS

Our experiments with the two-atom hydrogen molecule and the BHZ model reveal the applicability of digitized STA followed by sequential digitized adiabaticity in the determination of electronic states. Next, we investigate the ground state for $N(> 2)$-atom hydrogen chains [8]. Due to the restrictions of our current setup, it is difficult for us to reliably perform an $N(> 2)$-qubit experiment. Therefore, we only present the results of numerical simulation in this paper and the experimental implementation will be performed in the future.

The Hamiltonian of an N-atom hydrogen chain is written as

$$H(N; R) = g_0(R) + \sum_{i=1}^{N} g(R)Z_i + \sum_{i=1}^{N-1} g_{12}(R)Y_i Y_{i+1}, \qquad (22)$$

where R is the internuclear distance between each pair of two adjacent hydrogen atoms. For simplicity, the R dependencies of $g_0(R)$, $g(R)$, and $g_{12}(R)$ are assumed to be the same as those in the two-atom hydrogen molecule. (1) For the specified distance ($R = R_0 = 0.05$ Å), the initial Hamiltonian is set to be $H_0 = H(N - 1; R_0) + g(R_0)Z_N$ and the adiabatic Hamiltonian reads $H_{ad}(t) = H(N - 1; R_0) + g(R_0)Z_N + \lambda(t)g_{12}(R_0)Y_{N-1}Y_N$. The initial state is set to be $|\Psi(0)\rangle = |\varphi_0(N - 1; R_0)\rangle \otimes |0\rangle$, where the ground state $|\varphi_0(N - 1; R_0)\rangle$ of the $(N - 1)$-atom chain is predetermined. The adiabatic process is digitized into

$$U_m = R_{Y_1 Y_2}(\theta_{m;3}) \cdots R_{Y_{N-2} Y_{N-1}}(\theta_{m;3}) R_{Y_{N-1} Y_N}(\theta_{m;2}) R_{Z_1}$$
$$(\theta_{m;1}) \cdots R_{Z_N}(\theta_{m;1}), \qquad (23)$$

where $\theta_{m;1} = 2g(R_0)\Delta t$, $\theta_{m;2} = 2g_{12}(R_0)\lambda(m\Delta t)\Delta t$ and $\theta_{m;3} = 2g_{12}(R_0)\Delta t$. (2) For the other distances ($R > R_0$), a sequential digitized adiabatic protocol is applied to the same distance sequence, $\{R_0 = 0.05 \text{ Å}, R_1 = 0.15 \text{ Å}, \ldots, R_{16} = 1.65 \text{ Å}\}$, as in Sec. A. At each ith distance, the initial Hamiltonian is selected to be $H_0 = c(R_i)H(N; R_{i-1})$ and the adiabatic Hamiltonian is given accordingly by $H_{ad}(t) = c(R_i)H(N; R_{i-1}) + \lambda(t)[H(N; R_i) - c(R_i)H(N; R_{i-1})]$. The initial state $|\varphi_0(N; R_{i-1})\rangle$ is predetermined at the previous $(i - 1)$th distance. For the digitized adiabatic operator, $U_{ad} =$
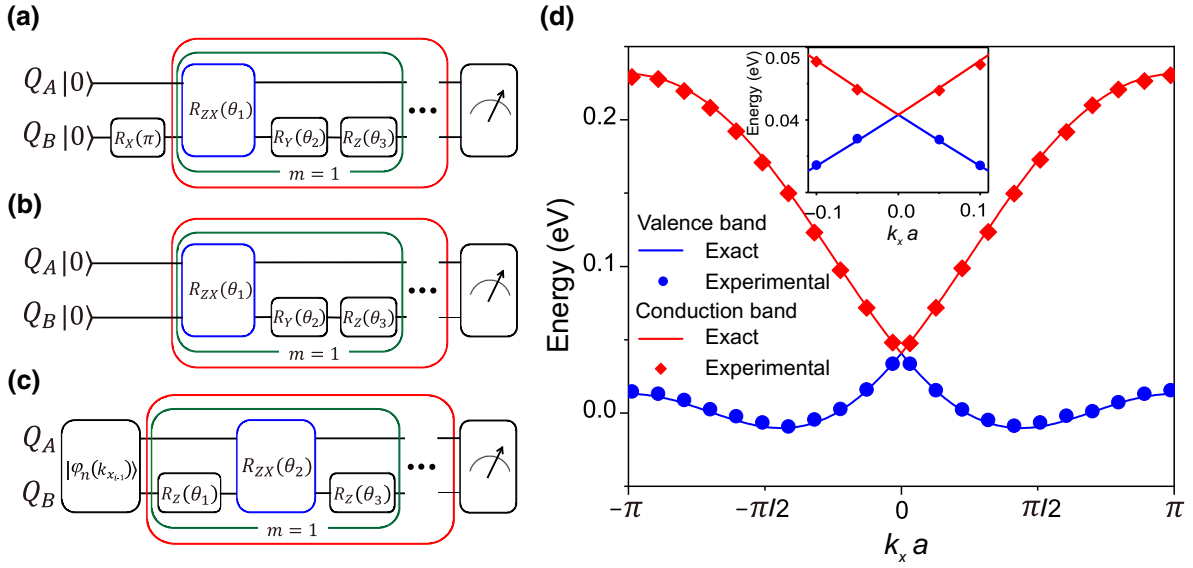
FIG. 6. The BHZ-model experiment. (a),(b) The quantum circuit diagrams of digitized STA to determine the ground and excited eigenstates at the starting wave vectors, $k_{x_0} = \pm 0.1a^{-1}, \pm 3.1a^{-1}$. (c) The quantum circuit diagram of sequential digitized adiabaticity for other wave vectors, $k_x \neq k_{x_0}$. (d) The experimental determination of the valence and conduction bands along the X-Γ-X line cut. The inset is an enlarged view of (d) around the Dirac point. The symbols (circles and diamonds) represent the experimental results, while the solid lines represent the exact results from the theoretical calculation.

$U_M \cdots U_m \cdots U_1$, each partial time evolution is given by

$$U_m = R_{Y_1 Y_2}(\theta_{m;2}) \cdots R_{Y_{N-1} Y_N}(\theta_{m;2}) R_{Z_1}(\theta_{m;1}) \cdots R_{Z_N}(\theta_{m;1}), \tag{24}$$

where $\theta_{m;1} = 2g_\lambda(m\Delta t)\Delta t$ and $\theta_{m;2} = 2g_{12}(R_i)\Delta t$. The adiabatic operation time is in the range $0.1 \leq gT \leq 0.9$, while the number of digitized steps is in the range $3 \leq M \leq 10$. In general, the value of M increases with the increase of the chain length N and the internuclear distance R. The ground-state energy landscapes (ε_0 versus R) obtained for the N-atom hydrogen chains ($3 \leq N \leq 6$) are plotted in Figs. 7(a)–7(d). Through a series of sequential numerical simulations from the three- to six-atom chains, we successfully determine the structure of the electronic ground states. The state fidelities from the numerical simulation are $\gtrsim 99\%$ at short internuclear distances and still $\gtrsim 95\%$ for 1.05 Å $\leq R_i \leq 1.65$ Å. Although the numerical study in this paper is limited to the ground states of multiatom hydrogen chains, the same strategy is valid for the determination of the excited states. In addition, we can extend the current chain model with two-qubit interactions to a more complicated one with multiqubit interactions. Our method of digitized STA and sequential digitized adiabaticity is expected to be available for the determination of various eigenstates.

V. SUMMARY AND CONCLUSIONS

In this paper, we apply an eigensolver of digitized STA and sequential digitized adiabaticity to determine the

electronic states of various systems. For the two-atom hydrogen molecule and the topological BHZ model, the state determination is experimentally implemented in a two-qubit superconducting device.

(1) In the case of the hydrogen molecule, we select an internuclear distance at $R = R_0 = 0.05$ Å with a weak interqubit interaction. Two uncoupled Hamiltonians are set to be the initial Hamiltonians H_0 and the counterdiabatic Hamiltonians $H_{cd}(t)$ are estimated under the single-qubit assumption. Both the ground ($|\varphi_0(R = R_0)\rangle$) and first excited ($|\varphi_1(R = R_0)\rangle$) states are experimentally determined by the four-step digitized STA (state fidelities $\mathcal{F} \approx 99\%$ and 98%). Subsequently, we set a sequence of internuclear distances, $\{R_0 = 0.05$ Å$, R_1 = 0.15$ Å$, \ldots, R_{16} = 1.65$ Å$\}$. For each ith distance R_i, the initial Hamiltonian is set to be $H(R_{i-1})$ at the $(i-1)$th distance. With the initial states at $|\varphi_0(R_{i-1})\rangle$ and $|\varphi_1(R_{i-1})\rangle$, an M-step digitized adiabatic process is implemented to experimentally determine the ground and first excited states, $|\varphi_0(R_i)\rangle$ and $|\varphi_1(R_i)\rangle$. Through such sequential digitized adiabaticity, the potential energy landscape of H_2 is extracted with a high degree of accuracy, with state fidelities in the range 94–99%.

(2) The same strategy is applied to the BHZ model to experimentally determine the valence and conduction bands along the X-Γ-X line cut ($k_y = 0$) of the FBZ. For the two sets of starting wave vectors k_{x_0}, the ground and excited states, $|\varphi_0(k_{x_0})\rangle$ and $|\varphi_1(k_{x_0})\rangle$, are extracted by four-step digitized STA under the single-qubit
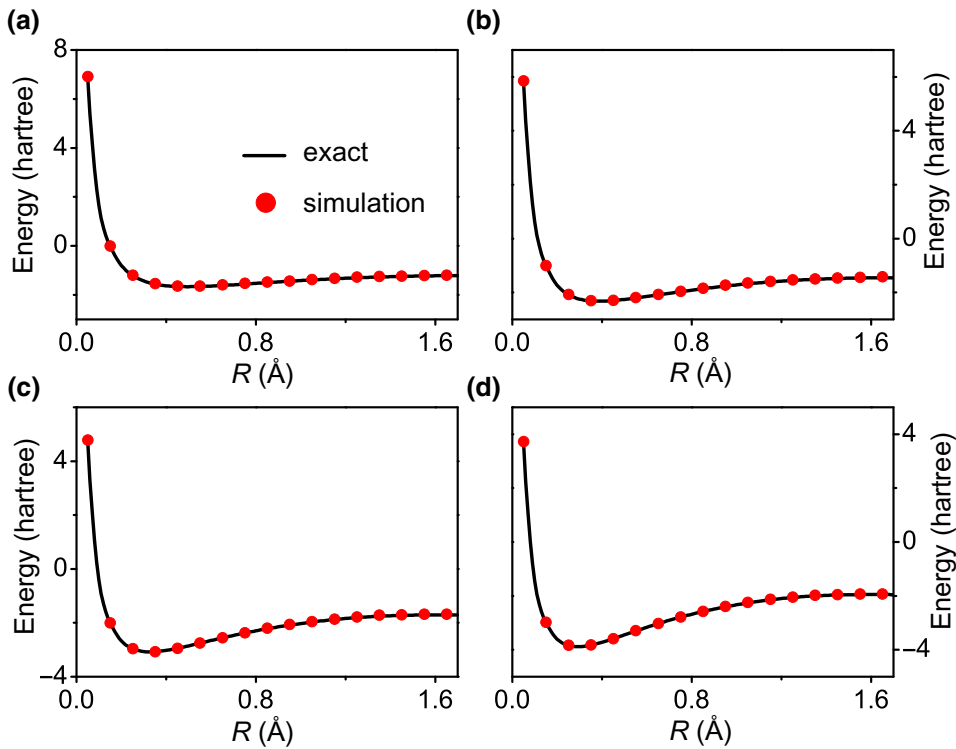
FIG. 7. The ground-state energy landscapes of the (a) three-, (b) four-, (c) five-, and (d) six-atom hydrogen chains, where R is the internuclear distance between two adjacent atoms. The red circles are obtained from the numerical simulation of digitized STA and sequential digitized adiabaticity, while the black solid lines are the exact results.

approximation. Through various sequences of wave vectors, $\{k_{x_0}, \ldots, k_{x_i}, \ldots\}$, the electronic structure $|\varphi_{n=0,1}(k_{x_i})\rangle$ along the X-Γ-X line cut is obtained using sequential digitized adiabaticity, showing high state fidelities (98–99%). A linear dispersion relation, $\delta\varepsilon_n(k_x) \propto k_x$, is also experimentally confirmed around the Dirac point ($k_x = 0$).

(3) This eigensolver approach is then extended to the N-atom hydrogen chains by a numerical simulation. With the predetermined ground state $|\varphi_0(N = 2; R_0)\rangle$ of the two-atom hydrogen molecule, a series of sequential digitized adiabatic processes are applied. For the specified internuclear distance $R = R_0$, the simulation procedure follows $|\varphi_0(N = 2; R_0)\rangle \rightarrow |\varphi_0(N = 3; R_0)\rangle \rightarrow \cdots$. For other distances ($R > R_0$) at a given chain length (N), the simulation procedure follows $|\varphi_0(N; R_0)\rangle \rightarrow |\varphi_0(N; R_1)\rangle \rightarrow \cdots$. The overall state fidelities for the conditions of $3 \leq N \leq 6$ and $0.05\,\text{Å} \leq R \leq 1.65\,\text{Å}$ are around 95–99%.

Our experiments and numerical simulations confirm the applicability of digitized STA followed by sequential digitized adiabaticity. Conceptually speaking, this approach aims to determine the eigenstates $|\varphi_n\rangle$ of a quantum system in a parameter (Λ) space. In the first step, we select one or a few starting points (Λ_0) with weak interqubit interactions. With nearly zero information about $|\varphi_n(\Lambda_0)\rangle$, a good strategy is to drag the system from a simple eigenstate (e.g., a product state with respect to an uncoupled Hamiltonian) to the target eigenstate via the digitized STA. Subsequently, we set sequences of $\{\Lambda_0, \Lambda_1, \ldots, \Lambda_i, \ldots\}$,

to traverse the parameter space. Due to the short state distance, digitized adiabaticity can be applied to sequentially drag the system from $|\varphi_n(\Lambda_{i-1})\rangle$ to $|\varphi_n(\Lambda_i)\rangle$ with a high fidelity. This approach is in parallel with the standard solver of a differential equation. For example, a time-dependent function $f(t)$ can be sequentially determined by $f(t_0) \rightarrow f(t_0 + \Delta t) = f(t_0) + f'(t_0)\Delta t \rightarrow \cdots$. Theoretically speaking, we expect that this method can be applicable to the eigenstructure ($|\varphi_n(\Lambda)\rangle$ and $\varepsilon_n(\Lambda)$) of a large system with a good efficiency and a high fidelity. However, the error accumulation through multiple adiabatic steps could limit the output fidelity, so that future experiments on large qubit devices would be necessary.

APPENDIX A: SINGLE-QUBIT APPROXIMATION

The adiabatic Hamiltonian of an N-qubit system can, in general, be expanded into

$$H_{\mathrm{ad}}(t) = g^{(0)}(t) + \sum_{i=1}^{N}\sum_{j=1}^{3} g_{ij}^{(1)}(t)\sigma_i^j$$

$$+ \sum_{i,k=1}^{N}\sum_{j,l=1}^{3} g_{ij,kl}^{(2)}(t)\sigma_i^j \sigma_k^l + \cdots, \tag{A1}$$

where $\{\sigma_i^j = X_i, Y_i, Z_i\}$ are the Pauli matrices acting on qubit i. In our experiment, Eq. (A1) is truncated up to the second order with nonzero coefficients in $\{g^{(0)}(t), g_{ij}^{(1)}(t), g_{ij,kl}^{(2)}(t)\}$. To circumvent the instantaneous eigenstates in the counterdiabatic Hamiltonian, we apply a single-qubit approximation to the multiqubit interaction, e.g., $\sigma_i^j \sigma_k^l \approx \sigma_i^j + \sigma_k^l$ [33]. The adiabatic Hamiltonian in Eq. (A1) is decomposed into $H_{\mathrm{ad}}(t) \rightarrow g^{(0)}(t) + \sum_{i=1}^{N} H_{\mathrm{ad};i}(t)$, where $H_{\mathrm{ad};i}(t) = \vec{h}_i(t) \cdot \vec{\sigma}_i/2$. For conciseness, we introduce the vector of Pauli matrices, $\vec{\sigma}_i = X_i\vec{e}_1 + Y_i\vec{e}_2 + Z_i\vec{e}_3$, where $\{\vec{e}_{j=1,2,3}\}$ is the set of three unit vectors. The three components of the coefficient vector $\vec{h}_i(t)$ are given by $h_{i;j=1,2,3}(t) = g_{ij}^{(1)}(t) + \sum_{k,l} g_{ij,kl}^{(2)}(t)$. For the ith qubit, its counterdiabatic Hamiltonian is approximated as

$$H_{\mathrm{cd};i}(t) \approx \frac{\vec{h}_i(t) \times \dot{\vec{h}}_i(t)}{2|\vec{h}_i(t)|^2} \cdot \vec{\sigma}_i. \tag{A2}$$

The overall counterdiabatic Hamiltonian is approximated as $H_{\mathrm{cd}}(t) \approx \sum_{i=1}^{N}\sum_{j=1}^{3} g_{\mathrm{cd};ij}(t)\sigma_i^j$. With the exact adiabatic and the approximate counterdiabatic parts, the total Hamiltonian for the subsequent digitized treatment is given by

$$H_{\mathrm{tot}}(t) \approx g^{(0)}(t) + \sum_{i=1}^{N}\sum_{j=1}^{3}[g_{i,j}^{(1)}(t) + g_{\mathrm{cd};i,j}(t)]\sigma_i^j$$

$$+ \sum_{i,k=1}^{N}\sum_{j,l=1}^{3} g_{i,j;k,l}^{(2)}(t)\sigma_i^j \sigma_k^l. \tag{A3}$$

APPENDIX B: BRAVYI-KITAEV MAPPING

After the second quantization, the electronic Hamiltonian of the hydrogen molecule is formally written as

$$H = \mathcal{E}_{\mathrm{nucl}} + \sum_{i,j} h_{ij} a_i^+ a_j + \sum_{i,j,k,l} h_{ijkl} a_i^+ a_j^+ a_k a_l, \tag{B1}$$

where h_{ij} and h_{ijkl} are one- and two-electron integrals. Next, we apply the Bravyi-Kitaev transformation [43],

where the fermion annihilation and creation operators are reformulated as

$$a_i = \left[X_{U(i)}X_i Z_{P(i)} + iX_{U(i)}Y_i Z_{\rho(i)} \right]/2, \tag{B2}$$

$$a_i^+ = \left[X_{U(i)}X_i Z_{P(i)} - iX_{U(i)}Y_i Z_{\rho(i)} \right]/2. \tag{B3}$$

Here, $U(i)$, $P(i)$, and $R(i)$ are the update, parity, and remainder sets, respectively, and their explicit lists can be found in Ref. [43]. The other set $\rho(i)$ is determined by $\rho(i) = P(i)$ for $i \in$ even and $\rho(i) = R(i)$ for $i \in$ odd. Through a straightforward derivation, the Hamiltonian in Eq. (B1) is simplified to

$$H = g_0 I + g_1 Z_A + g_2 Z_B + g_3 Z_A Z_B + g_4 X_A X_B + g_5 Y_A Y_B, \tag{B4}$$

where the coefficients satisfy $g_1 = g_2$ and $g_4 = g_5$. The extra condition of $|g_4| \gg |g_3|$ indicates that the three two-qubit couplings can be efficiently simulated by $X_A X_B$ or $Y_A Y_B$. In our experiment, we choose the latter two-qubit operator and the Hamiltonian is approximated as

$$H = g_0 + g(Z_A + Z_B) + g_{12} Y_A Y_B. \tag{B5}$$

The explicit dependence between $\{g_0, g, g_{12}\}$ and the internuclear distance R in our experiment is cited from Ref. [9].

---

[1] M. A. Nielsen and I. L. Chuang, *Quantum Computation and Quantum Information* (Cambridge University Press, Cambridge, England, 2010).

[2] A. A. Houck, H. E. Türeci, and J. Koch, On-chip quantum simulation with superconducting circuits, Nat. Phys. **8**, 292 (2012).

[3] I. M. Georgescu, S. Ashhab, and F. Nori, Quantum simulation, Rev. Mod. Phys. **86**, 153 (2014).

[4] Google AI Quantum, Quantum supremacy using a programmable superconducting processor, Nature **574**, 505 (2019).

[5] A. Peruzzo, J. McClean, P. Shadbolt, M. Yung, X. Zhou, P. J. Love, A. Aspuru-Guzik, and J. L. O'Brien, A variational eigenvalue solver on a photonic quantum processor, Nat. Commun. **5**, 4213 (2014).

[6] P. J. J. O'Malley, R. Babbush, I. D. Kivlichan, J. Romero, J. R. McClean, R. Barends, J. Kelly, P. Roushan, A. Tranter, and N. Ding *et al.*, Scalable Quantum Simulation of Molecular Energies, Phys. Rev. X **6**, 031007 (2016).

[7] A. Kandala, A. Mezzacapo, K. Temme, M. Takita, M. Brink, J. M. Chow, and J. M. Gambetta, Hardware-efficient variational quantum eigensolver for small molecules and quantum magnets, Nature **549**, 242 (2017).

[8] Google AI Quantum, Hartree-Fock on a superconducting qubit quantum computer, Science **369**, 1084 (2020).

[9] J. I. Colless, V. V. Ramasesh, D. Dahlen, M. S. Blok, M. E. Kimchi-Schwartz, J. R. McClean, J. Carter, W. A. de Jong, and I. Siddiqi, Computation of Molecular Spectra on a Quantum Processor with an Error-Resilient Algorithm, Phys. Rev. X **8**, 011021 (2018).

[10] E. Farhi, J. Goldstone, S. Gutmann, J. Lapan, A. Lundgren, and D. Preda, A quantum adiabatic evolution algorithm applied to random instances of an NP-complete problem, Science **292**, 472 (2001).

[11] X. H. Peng, Z. Y. Liao, N. Y. Xu, G. Qin, X. Y. Zhou, D. Suter, and J. F. Du, Quantum Adiabatic Algorithm for Factorization and its Experimental Implementation, Phys. Rev. Lett. **101**, 220405 (2008).

[12] A. Das and B. K. Chakrabarti, Colloquium: Quantum annealing and analog quantum computation, Rev. Mod. Phys. **80**, 1061 (2008).

[13] A. P. Young, S. Knysh, and V. N. Smelyanskiy, First-Order Phase Transition in the Quantum Adiabatic Algorithm, Phys. Rev. Lett. **104**, 020502 (2010).

[14] M. W. Johnson, M. H. Amin, S. Gildert, T. Lanting, F. Hamze, N. Dickson, R. Harris, A. J. Berkley, J. Johansson, and P. Bunyk *et al.*, Quantum annealing with manufactured spins, Nature **473**, 194 (2011).

[15] S. Boixo, T. Albash, F. M. Spedalieri, N. Chancellor, and D. A. Lidar, Experimental signature of programmable quantum annealing, Nat. Commun. **4**, 1 (2013).

[16] L. Veisa and J. Pittner, Adiabatic state preparation study of methylene, J. Chem. Phys. **140**, 214111 (2014).

[17] C. Hu, A. C. Santos, J. Cui, Y. Huang, D. O. Soares-Pinto, M. S. Sarandy, C. Li, and G. Guo, Quantum thermodynamics in adiabatic open systems and its trapped-ion experimental realization, npj Quantum Inf. **6**, 73 (2020).

[18] M. Steffen, W. Dam, T. Hogg, G. Breyta, and Isaac Chuang, Experimental Implementation of an Adiabatic Quantum Optimization Algorithm, Phys. Rev. Lett. **90**, 067903 (2003).

[19] B. P. Lanyon, C. Hempel, D. Nigg, M. Müller, R. Gerritsma, F. Zähringer, P. Schindler, J. T. Barreiro, M. Rambach, and G. Kirchmair *et al.*, Universal digital quantum simulation with trapped ions, Science **334**, 6052 (2011).

[20] Y. Salathé, M. Mondal, M. Oppliger, J. Heinsoo, P. Kurpiers, A. Potocnik, A. Mezzacapo, U. Las Heras, L. Lamata, and E. Solano *et al.*, Digital Quantum Simulation of Spin Models with Circuit Quantum Electrodynamics, Phys. Rev. X **5**, 021027 (2015).

[21] R. Barends, A. Shabani, L. Lamata, J. Kelly, A. Mezzacapo, U. L. Heras, R. Babbush, A. G. Fowler, B. Campbell, and Yu Chen *et al.*, Digitized adiabatic quantum computing with a superconducting circuit, Nature **534**, 222 (2016).

[22] M. V. Berry, Transitionless quantum driving, J. Phys. A: Math. Theor. **42**, 365303 (2009).

[23] X. Chen, I. Lizuain, A. Ruschhaupt, D. Guéry-Odelin, and J. G. Muga, Shortcut to Adiabatic Passage in Two- and Three-Level Atoms, Phys. Rev. Lett. **105**, 123003 (2010).

[24] K. Takahashi, Shortcuts to adiabaticity for quantum annealing, Phys. Rev. A **95**, 012309 (2017).

[25] D. Guéry-Odelin, A. Ruschhaupt, A. Kiely, E. Torrontegui, S. Martínez-Garaot, and J. G. Muga, Shortcuts to adiabaticity: Concepts, methods, and applications, Rev. Mod. Phys. **91**, 045001 (2019).

[26] J. Zhang, T. Kyaw, D. M. Tong, E. Sjöqvist, and Leong-Chuan Kwek, Fast non-Abelian geometric gates via transitionless quantum driving, Sci. Rep. **5**, 18414 (2016).

[27] Z. Zhang, T. Wang, L. Xiang, J. Yao, J. Wu, and Y. Yin, Measuring the Berry phase in a superconducting phase qubit by a shortcut to adiabaticity, Phys. Rev. A **95**, 042345 (2017).

[28] T. Wang, Z. Zhang, L. Xiang, Z. Jia, P. Duan, W. Cai, Z. Gong, Z. Zong, M. Wu, J. Wu, L. Sun, Y. Yin, and G. Guo, The experimental realization of high-fidelity shortcut-to-adiabaticity quantum gates in a superconducting Xmon qubit, New J. Phys. **20**, 065003 (2018).

[29] Z. Zhang, T. Wang, L. Xiang, Z. Jia, P. Duan, W. Cai, Z. Zhan, Z. Zong, J. Wu, L. Sun, Y. Yin, and G. Guo, Experimental demonstration of work fluctuations along a shortcut to adiabaticity with a superconducting Xmon qubit, New J. Phys. **20**, 085001 (2018).

[30] T. Wang, Z. Zhang, L. Xiang, Z. Gong, J. Wu, and Y. Yin, Simulating a topological transition in a superconducting phase qubit by fast adiabatic trajectories, Sci. China Phys. Mech. Astron. **61**, 047411 (2018).

[31] A. C. Santos and M. S. Sarandy, Generalized shortcuts to adiabaticity and enhanced robustness against decoherence, J. Phys. A: Math. Theor. **51**, 025301 (2018).

[32] A. Smith, Y. Lu, S. An, X. Zhang, J. Zhang, Z. Gong, H. T. Quan, C. Jarzynski, and K. Kim, Verification of the quantum nonequilibrium work relation in the presence of decoherence, New J. Phys. **20**, 013008 (2018).

[33] N. N. Hegade, K. Paul, Y. Ding, M. Sanz, F. Albarran-Arriagada, E. Solano, and X. Chen, Shortcuts to Adiabaticity in Digitized Adiabatic Quantum Computing, Phys. Rev. Appl. **15**, 024038 (2021).

[34] P. W. Claeys, M. Pandey, D. Sels, and A. Polkovnikov, Floquet-Engineering Counterdiabatic Protocols in Quantum Many-Body Systems, Phys. Rev. Lett. **123**, 090602 (2019).

[35] X. Chen, A. Ruschhaupt, S. Schmidt, A. del Campo, D. Guéry-Odelin, and J. G. Muga, Fast Optimal Frictionless Atom Cooling in Harmonic Traps: Shortcut to Adiabaticity, Phys. Rev. Lett. **104**, 063002 (2010).

[36] H. F. Trotter, On the product of semigroups of operators, Proc. Amer. Math. Soc. **10**, 545 (1959).

[37] M. Suzuki, Generalized Trotter's formula and systematic approximants of exponential operators and inner derivations with applications to many-body problems, Commun. Math. Phys. **51**, 183 (1976).

[38] S. Lloyd, Universal quantum simulators, Science **273**, 1073 (1996).

[39] R. Barends, L. Lamata, J. Kelly, L. García-Álvarez, A. G. Fowler, A. Megrant, E. Jeffrey, T. C. White, D. Sank, and J. Y. Mutus *et al.*, Digital quantum simulation of fermionic models with a superconducting circuit, Nat. Commun. **6**, 7654 (2015).

[40] B. A. Bernevig, T. L. Hughes, and S. C. Zhang, Quantum spin Hall effect and topological phase transition in HgTe quantum wells, Science **314**, 1757 (2006).

[41] T. Wang, Z. Zhang, L. Xiang, Z. Jia, P. Duan, Z. Zong, Z. Sun, Z. Dong, J. Wu, Y. Yin, and G. Guo, Experimental Realization of a Fast Controlled-*Z* Gate via a Shortcut to Adiabaticity, Phys. Rev. Appl. **11**, 034030 (2019).

[42] L. Xiang, Z. Zong, Z. Sun, Z. Zhan, Y. Fei, Z. Dong, C. Run, Z. Jia, P. Duan, J. Wu, Y. Yin, and G. Guo, Random Walk on the Bloch Sphere Realized by a Simultaneous Feedback and Feed-Forward Control in a Superconducting Xmon Qubit, Phys. Rev. Appl. **14**, 014099 (2020).

[43] J. T. Seeley, M. J. Richard, and P. J. Love, The Bravyi-Kitaev transformation for quantum computation of electronic structure, J. Chem. Phys. **137**, 224109 (2012).

[44] V. V. Shende, I. L. Markov, and S. S. Bullock, Minimal universal two-qubit controlled-NOT-based circuits, Phys. Rev. A **69**, 062321 (2004).

[45] H. Jiang, L. Wang, Q. F. Sun, and X. C. Xie, Numerical study of the topological Anderson insulator in HgTe/CdTe quantum wells, Phys. Rev. B **80**, 165316 (2009).